JGR Atmospheres

RESEARCH ARTICLE
10.1029/2018JD030087

The Characteristics of Tropical and Midlatitude Mesoscale Convective Systems as Revealed by Radar Wind Profilers

Die Wang[1], Scott E. Giangrande[1], Kathleen A. Schiro[2], Michael P. Jensen[1], and Robert A. Houze, Jr.[3,4]

[1]Environmental and Climate Sciences Department, Brookhaven National Laboratory, Upton, NY, USA, [2]Jet Propulsion Laboratory, California Institute of Technology, Pasadena, CA, USA, [3]Pacific Northwest National Laboratory, Richland, WA, USA, [4]Department of Atmospheric Sciences, University of Washington, Seattle, WA, USA

Abstract This study contrasts characteristics of mature squall-line mesoscale convective systems (MCSs) observed by extended ground-based radar wind profiler (RWP) deployments from the U.S. Department of Energy Atmospheric Radiation Measurement program. This analysis compares the dynamical structure, precipitation, and cold pool properties associated with MCS events over RWP sites in Oklahoma, USA, (midlatitude) to those observed during a 2-year RWP deployment to Manaus, Brazil, during GoAmazon2014/5 campaign (tropical). The MCSs indicate similar convective line rainfall rates and total rainfall accumulations. However, midlatitude events suggest a larger fractional stratiform contribution to total precipitation. For both regions, convective line cold pools are associated with sharp decreases (approximately 10 K) in the surface equivalent potential temperature (θ_e) near the time of line passage. Surface θ_e properties for both regions suggest a modest relationship between rainfall rate and the probability of observing measurable surface rainfall. The probability of observing convective updrafts in both tropical and midlatitude MCS events is found to be similar as a function of low-level radar reflectivity. However, midlatitude MCSs are associated with more intense convective updrafts, with upward air motions (mean, maximum) peaking at higher altitude. The most pronounced contrast is the propensity for deeper and more intense downdrafts in midlatitude MCSs. An analysis based on observed downdraft properties is performed using simple mixing assumptions. For these events, the vertical gradient of θ_e in the lower troposphere is relatively consistent between the Amazon and Oklahoma, suggesting similar mixing rates for downdrafts originating below 3 km (0.1 km^{-1}). However, if downdrafts originate nearer to the level of minimum θ_e at SGP, mixing may be occurring at rates comparable to 0.3 km^{-1}.

Key Points:
- Mesoscale systems in Amazonia and Oklahoma have similar rain rates, cold pool properties, and inferred mixing rates for low-level downdrafts
- Mesoscale systems in Oklahoma show intense updrafts peaking at higher altitudes and greater stratiform rain fractions than Amazon systems
- Oklahoma systems produce strong downdrafts that occur more frequently at higher altitudes (up to 6 km with mixing) than Amazon systems

Supporting Information:
- Supporting Information S1

Correspondence to:
D. Wang,
diewang@bnl.gov

Citation:
Wang, D., Giangrande, S. E., Schiro, K., Jensen, M. P., & Houze, R. A. (2019). The characteristics of tropical and midlatitude mesoscale convective systems as revealed by radar wind profilers. *Journal of Geophysical Research: Atmospheres*, *124*, 4601–4619. https://doi.org/10.1029/2018JD030087

Received 29 NOV 2018
Accepted 18 MAR 2019
Accepted article online 29 MAR 2019
Published online 16 APR 2019

Author Contributions

Conceptualization: Die Wang
Methodology: Die Wang
Writing - Original Draft: Die Wang
Formal Analysis: Die Wang
Investigation: Die Wang, Scott E. Giangrande, Kathleen A. Schiro, Michael P. Jensen
Resources: Die Wang, Scott E. Giangrande
Supervision: Scott E. Giangrande
Visualization: Die Wang
Writing - review & editing: Scott E. Giangrande, Kathleen A. Schiro, Michael P. Jensen

1. Introduction

Deep convective clouds control atmospheric circulations, influencing remote cloud environments that feedback to climate sensitivity (e.g., Del Genio et al., 2012; Donner et al., 2016; Gettelman & Sherwood, 2016; Sanderson et al., 2008; Sherwood et al., 2014; Trenberth et al., 2009). Among the largest and most intense convective clouds, mesoscale convective systems (MCSs) help regulate the global energy and water cycles through their extensive cloud coverage and the exchange of latent heat (e.g., Fritsch et al., 1986; Hartmann et al., 1984; Houze, 2004; Houze Jr. 2018). For the tropics and during the midlatitude warm seasons, MCSs contribute a significant portion of the total rainfall (e.g., Del Genio & Kovari, 2002; Nesbitt et al., 2006; Roca et al., 2014). Under warming climate scenarios, convection-permitting models (CPMs) that allow more realistic MCS treatments in global climate models (GCMs) indicate an enhancement in the frequency of extreme MCS events over North America, associated with increases in maximum rainfall rates and flooding risks (Prein et al., 2017). Extended MCS summaries performed using the WSR-88D NEXRAD network also indicate an increase in the frequency and intensity of longer-lasting MCSs, attributed with the rise in extreme precipitation events (Feng et al., 2016).

Numerous studies have contributed to our understanding of MCSs and their interactions with the larger-scale environment and climate system (e.g., Houze, 2004; Houze Jr. 1989, 2018; Johnson & Hamilton, 1988; Leary & Houze, 1979; Parker & Johnson, 2000, 2004; Rotunno et al., 1988; Schumacher et al., 2004). Unfortunately, current GCMs do not properly simulate MCS role in our climate system, since relevant MCS

processes operate across GCM resolved and parameterized scales (e.g., Donner, 1993; Donner et al., 2001; Mapes et al., 2006; Moncrieff, 1992). Even as new computing resources allow CPM or cloud-resolving model capabilities to better resolve MCSs to global scales (e.g., Bretherton & Khairoutdinov, 2015; Leutwyler et al., 2016; Skamarock et al., 2014) and the rapid development of CPMs quickly led to many model-driven MCS process studies (e.g., Barnes & Houze Jr. 2016; Lafore & Moncrieff, 1989; Morrison et al., 2009; Skamarock et al., 1994; Trier & Sharman, 2009), inadequate observational constraints inhibit high-resolution convective model process improvement (e.g., Del Genio et al., 2012; Donner et al., 2016; Fan et al., 2017; Mrowiec et al., 2012; Varble et al., 2014). Perhaps the most fundamental property of deep convection is its vertical air motion, in the form of updraft and downdraft. The understanding of convective dynamics and microphysics depends critically on knowledge of these motions. Yet these motions are among the most difficult aspects of convection to measure and have consequently long been poorly documented by direct observations.

Historically, the best observations of deep convective updraft and downdraft velocity have been collected by aircraft (e.g., Byers & Braham, 1948; LeMone & Zipser, 1980; Stith et al., 2004; Zipser, 1977). However, the cost and hazards associated with operations in thunderstorms limits data availability (and therefore generalizability) as to the structure, intensity, and variability found with deeper convective drafts. For severe thunderstorms and MCSs, several studies instead draw from scanning Doppler radar for kinematic characteristics (e.g., Biggerstaff & Houze, 1991; Cifelli et al., 2002, 2004; Heymsfield & Schotz, 1985; Roux, 1988; Silva Dias et al., 2002; Smull & Houze, 1987). For 3-D wind field retrievals to scales O(>1 km), examples of multi-Doppler techniques applied to MCS events are also limited, primarily because suitable radar networks are uncommon outside of field campaigns (e.g., Collis et al., 2013; North et al., 2017). For higher-resolution column updraft sampling, profiling radars have also resurfaced as an alternative for statistical core size-intensity relationships and mass flux properties (e.g., Giangrande et al., 2013, 2016; Kumar et al., 2015; May & Rajopadhyaya, 1996, 1999; Williams, 2012). Radar wind profilers (RWPs) have been previously deployed for several MCS field campaigns to characterize the horizontal wind, vertical air motion, and precipitation structure (e.g., Atlas et al., 2003; Augustine & Zipser, 1987; Cifelli & Rutledge, 1994, 1998; Lerach et al., 2010; May & Keenan, 2005; May et al., 2002; May & Rajopadhyaya, 1996). When optimized for precipitation studies (e.g., Tridon et al., 2013), even nontraditional RWP applications allow high-resolution O(200 m to 1 km) and high-accuracy (1–2 m/s) vertical air motion retrievals into deeper convective cores.

This study presents an extended RWP application to help address deficiencies in our understanding of MCS kinematics and coupled precipitation processes. Our motivation is to further characterize MCS kinematic structure by exploring bulk MCS properties from two archetypal continental locations to demonstrate regional (midlatitude, tropical) and select seasonal variability. These characterizations are drawn from a multievent data set collected by the U.S. Department of Energy's (DOE) Atmospheric Radiation Measurement (ARM, Mather & Voyles, 2013) program field site in Oklahoma, USA, and Mobile Facility (Miller et al., 2016) deployment in the Amazon Basin. Emphasis for the current study is on composite mean vertical air motion profiles and normalized time-height characteristics for the passage of intense (e.g., rain rate > 10 mm/hr) and mature (e.g., precipitating line) stage MCSs over the RWPs. Our dynamic studies focus on the convective line regions of these events and do not emphasize the transition to weaker mesoscale updraft/downdraft features that are observed, yet more difficult to quantify reliably with current technologies (e.g., Houze Jr. 1977; Zipser, 1977). Our analysis on leading squall-line/trailing-stratiform organization events also reflects only a subset of the arrangements and/or process interactions associated with MCSs (e.g., Houze Jr. 2018) and is not intended to represent all modes or life cycle stages for midlatitude or tropical MCSs. Surface precipitation breakdowns (e.g., convective-stratiform precipitation) and cold pool properties for the two regions are discussed. These efforts include additional analyses following Schiro and Neelin (2018) on the effect of the MCSs on the surface thermodynamics, the origin height of MCS downdrafts, and discussions on regional and seasonal variability therein.

2. Data and Methods

The primary data set for this study considers continental-tropical MCS characteristics collected by the U.S. DOE ARM facility during its "Observations and Modeling of the Green Ocean Amazon 2014–2015" (herein, GoAmazon2014/5 or MAO) campaign near Manaus, Brazil, from March 2014 through December 2015 (e.g., Martin et al., 2017, 2016). The main MAO site in Manacapuru has many collocated ground-based sensors, including an RWP and meteorological state instruments. Radiosondes are launched daily from the site at 6-hr intervals. An overview of campaign instrumentation, for environmental and cloud profiling is found

in Giangrande et al. (2017). Additional coverage for MCS events was provided by System for the Protection of the Amazonia S-band surveillance radar, located at 3.15°S, 59.99°W, to ensure selection of convective lines passing over the MAO site (visual inspection). In total, 45 MCS events were identified for this deployment, with 24 "Wet" season (December through April), 10 "Dry" season (June through September), and 11 "Transitional" season (March, October, and November) examples (Table S1 in the supporting information). Amazon events also satisfy MCS criteria outlined in the complementary work by Schiro and Neelin (2018). These criteria include that MCS events have a surface equivalent potential temperature (θ_e) drop greater than 5 K within 30 min of line passage and a maximum precipitation rate exceeding 10 mm/hr within the convective line. The representativeness of thermodynamic profiles has been modified from the requirements used by Schiro and Neelin (2018) to selecting events having radiosonde launches in advance of the convective line/cold pool that are launched less than 4 hr prior to line passage over the RWP.

A complementary midlatitude MCS data set was collected at the ARM Southern Great Plains (SGP) supersite near Lamont Oklahoma, USA (Sisterson et al., 2016). These observations are selected from the period between 2012 and 2016, when four RWPs continuously operated at the site (three at extended facilities, one at the Central Facility [CF] in Lamont, OK). Further information on the distributed ARM SGP radar facility, including site maps for RWP placement, are found in Jensen et al. (2016) and North et al. (2017). Sixteen SGP MCS cases were selected following the criteria outlined for Amazon events. Although data were not always available from all four RWPs for each SGP event, events always included the data from two RWP locations. We provide a list of SGP events in Table S2, including the additional storm information.

The ARM RWPs operate at ultrahigh frequencies (300 MHz to 3 GHz) and have been reconfigured to allow precipitation sampling that frequently points vertically and collect data through the depth of deep convective cells (to 17 km, e.g., Tridon et al., 2013). Domestic and international ARM RWPs operate at different frequencies (e.g., 1290 MHz for GoAmazon2014/5 and 915 MHz at SGP); however, these sampling differences are negligible as the primary radar quantities of interest are collected from precipitation (Rayleigh scatterers) and RWP measurements are not attenuated in rain. The ARM RWPs have a modest beam width (approximately 9°) and observe time-height estimates for the radar reflectivity factor (Z) and mean Doppler velocity at approximately 10-s temporal and 200-m gate resolution. Convective core and periphery vertical air velocity estimates follow retrieval methods performed by Giangrande et al. (2013, 2016). The Amazon retrievals were performed using a different fall speed relationship (Giangrande et al., 2016, their Figure 5) than the original SGP methodology (Giangrande et al., 2013), which assumes a higher propensity for small, faster-falling mixed phase particles in Amazon events. During this retrieval approach, RWP columns are designated as "convective" or "stratiform" based on an echo classification method from Williams et al. (1995) and Giangrande et al. (2013, 2016). Additional interpretation of these RWP classifications is found in the GoAmazon2014/5 surface drop size distribution and rainfall studies performed by Wang et al. (2018).

Standard ARM meteorological instrumentation at the SGP CF and GoAmazon2014/5 MAO site provide 1-min observations of quantities including the air temperature, relative humidity, and rainfall rate. The θ_e is estimated following Bolton (1980). Thermodynamic profiles are obtained from radiosondes following standard ARM processing (Vaisala RS-92 radiosondes [Jensen et al., 2015]). For composite MCS characteristics, we present in the following sections, MCSs are aligned in time by using the time of the maximum surface rainfall rate (R; time = 0). The approach is similar to the compositing performed by Schiro and Neelin (2018) that was accomplished using a reference time associated with the minimum in θ_e attributed to the convective cold pool. For both data sets, the choice of maximum R or the use of the minimum in θ_e yields similar results (not shown). This decision to use R was necessary to include observations from the satellite RWP locations around the SGP CF that did not have the collocated instrumentation to estimate θ_e.

3. Overview of MCS Composite Characteristics

3.1. Thermodynamic and Precipitation Profile Behaviors

In Figure 1, we show the composite Skew-T Log-P diagrams from the radiosondes launched prior to convective lines for MAO and SGP MCSs. Shading on these composites indicates areas associated with composite convective available potential energy (CAPE, red) and convective inhibition (CIN, blue). Surface parcels for CAPE and CIN estimates are defined by the level of the maximum virtual temperature in the lowest kilometer. This represents the most buoyant parcel in the boundary layer and maximizes the calculated values. Thus, the shadings are comparable to "most unstable" CAPE/CIN (MUCAPE/MUCIN), as reported in

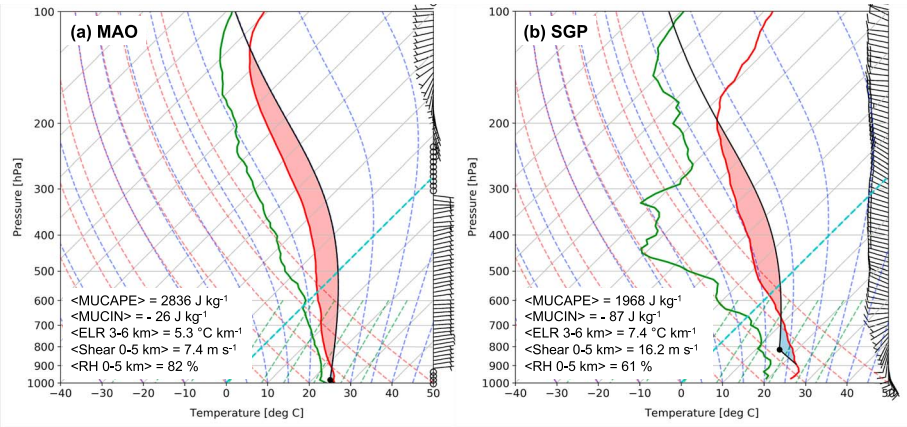

Figure 1. Composite skew-*T* log-*P* diagrams from radiosondes launched prior to convective lines for Amazon (MAO; a) and Oklahoma (SGP; b) mesoscale convective systems. The green solid lines are dew point temperature profiles. The red solid lines are environment temperature profiles. The black solid lines are the temperature profiles of the air parcel. Shading areas are the most unstable CAPE (MUCAPE; red) and the most unstable CIN (MUCIN; blue). Mean MUCAPE, MUCIN, environmental lapse rate (ELR), mean low level wind shear, and mean relative humidity (RH) below 5 km are also indicated.

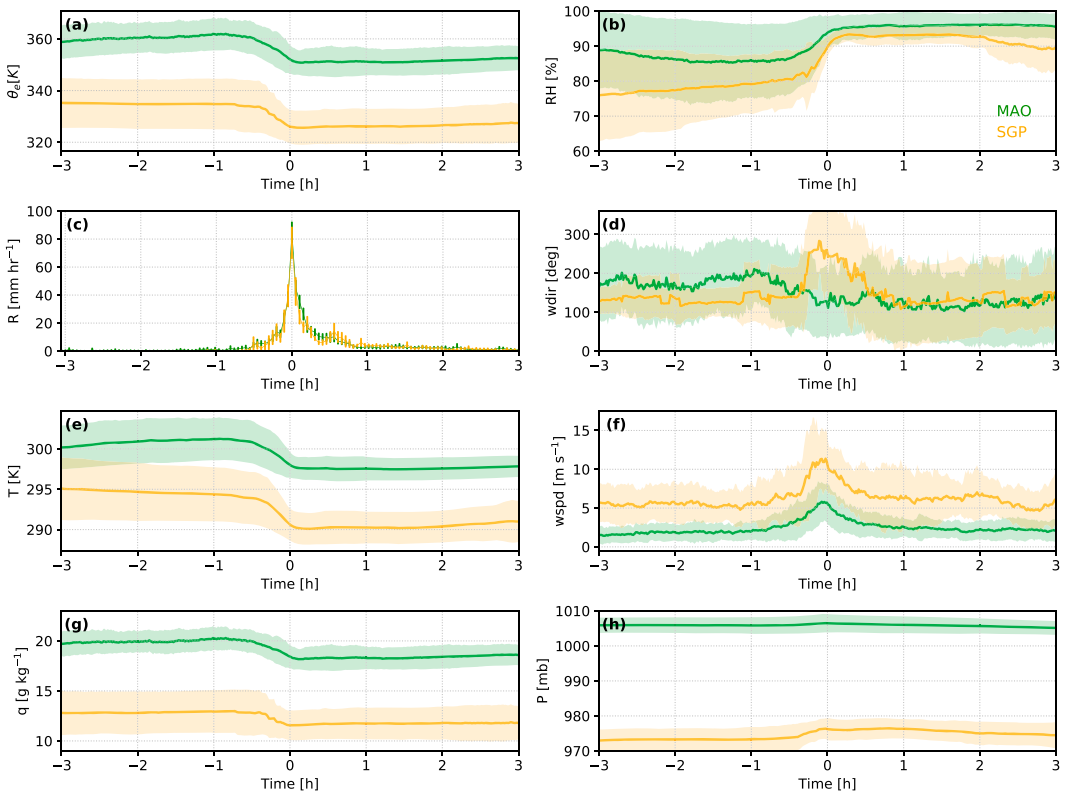

Figure 2. Composites of surface meteorological quantities (a) equivalent potential temperature θ_e, (b) relative humidity RH, (c) rainfall rate *R*, (d) wind direction, (e) dry bulb temperature *T*, (f) wind speed, (g) specific humidity *q*, and (h) barometric pressure *P*, at the Southern Great Plains (SGP; orange) and Amazon (MAO, green) sites. The time of the reference maximum rain rate is time 0. Shading and error bars reflect the ±1 standard deviation of each quantity.

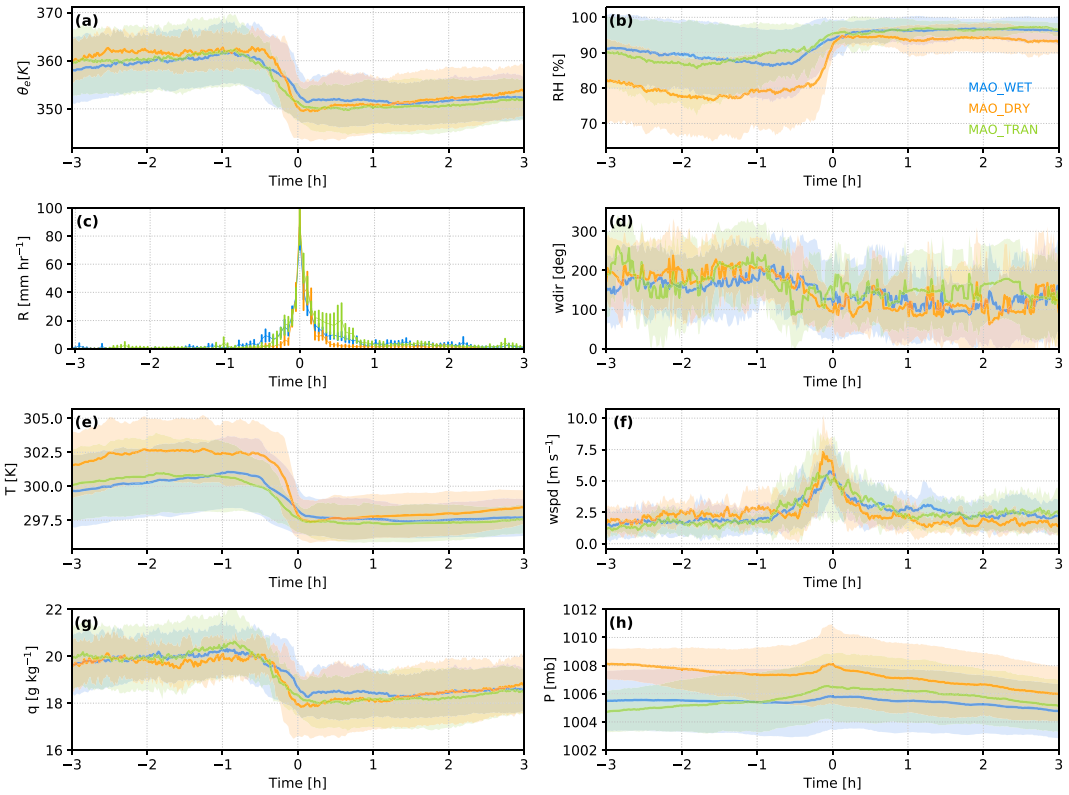

Figure 3. As in Figure 2, but for Amazon MCSs during Wet (MAO WET), Dry (MAO DRY), and Transational (MAO TRAN) seasons. MAO = GoAmazon2014/5 campaign.

Tables S1 and S2. Other basic convective forcing parameters are also calculated from these radiosondes following Jensen et al. (2015). The 0- to 5-km wind shear is typically higher at the SGP, while 0- to 5-km mean RH is substantially lower in the hours prior to convective line passage. The mean ELR is much steeper for the Oklahoma MCSs (7.4 °C/km) compared to the Amazon (5.3 °C/km) in the 3- to 6-km range, which could favor more intense convective vertical air motions for these SGP events. The Amazon sounding composite demonstrates a "skinny" CAPE profile throughout the depth of the troposphere compared to the SGP composite, with lower mean low-level CAPE (546 J/kg, 4 km above the level of free convection, to 684 J/kg at SGP) possibly indicative of more effective entrainment for MAO MCSs (e.g., Lucas et al., 1994; Lucas et al., 1994). For additional convenience, we plot histograms for SGP and MAO wind shear, MUCAPE, and MUCIN estimates in supporting information Figures S1 and S2.

In Figure 2, we composite (data set mean and standard deviation) surface thermodynamic quantities and rainfall rates over the set of MAO (green lines, shading) and SGP (orange lines, shading) MCS events. A listing for these events and their timing is provided in supporting information Tables S1 and S2. A similar composite for MAO MCS events separated according to Amazon seasonal regimes is shown in Figure 3. Event convective and stratiform precipitation accumulations (as designated using RWP echo classification methodologies) are reported in Tables S1 and S2.

Surface thermodynamic measurement composites in Figures 2 and 3 highlight key similarities and differences for regional/seasonal MCS characteristics. During MCS passage, the most prominent surface thermodynamic feature is that of the cold pool associated with these lines. As in Figures 2e and 2g and Figures 3e and 3g, we observe a rapid drop in the mean surface specific humidity (q) and temperature (T), around 1.5 (MAO) to 2 g/kg (SGP) and 4 (MAO) to 5 K (SGP), respectively. Although the starting surface conditions are different for each region, both data sets record a mean θ_e drop of approximately 10 K during this passage of the convective line (e.g., Figure 2a). The drop is also associated with an increase in the relative humidity (RH) at the leading edge of the cold pool, to a composite mean value of 96% for MAO and 93% for SGP (Figure 2b). The pressure increase (Figure 2h) we observe is smaller for the MAO events (mean of 1.4 mb) than for the SGP MCSs (mean of 3.5 mb). The surface wind field (Figures 2d and 2f) also adjusts in

response to the surface pressure rise (e.g., Engerer et al., 2008; Fujita, 1963; Schiro & Neelin, 2018; Vescio & Johnson, 1992). For MAO events, the wind shift is less pronounced, whereas SGP events are associated with frontal passages and winds shifting westerly behind these fronts.

To explore MCS cold pool properties further, we relate the precipitation, temperature, and specific humidity changes observed at the surface to the distribution of $\Delta\theta_e$ for the two sites (Figure 4). These comparisons help to bound downdraft behaviors we will explore in subsequent sections. In Figure 4a, we group surface precipitation rates in terms of coincident surface θ_e changes ($\Delta\theta_e$ increments set at 1 K, for 30-min intervals to within ±1 hr of the maximum R). The plot includes the probability for observing measurable precipitation (defined as surface $R > 2$ mm/hr) for our given $\Delta\theta_e$ bins (Figure 4b). In addition, we show the corresponding changes to the surface specific humidity and temperature in conjunction with the changes in θ_e (Figures 4c and 4d).

The MCS observations in Figure 4 suggest that the substantial decrease in surface θ_e occurs coincidently with the heaviest precipitation. The relationships we observe for SGP and MAO are consistent with previous Amazon results presented in Schiro and Neelin (2018). The lower bound observed for $\Delta\theta_e$ is recorded down to −15 K, is also associated with ΔT and Δq to −5 K and −3 g/kg, respectively. As found in Figure 2h, there is an increase in the surface pressure that is typically larger for SGP events. This agrees well with the indication that SGP MCS cold pools are associated with slightly larger decreases in temperature for a similar value of $\Delta\theta_e$ (e.g., Figure 4d) and that drier midlevel environments are favorable for additional evaporative cooling for similar precipitation. Nevertheless, the similarity between the MCS observations to include the modest correlations between R and $\Delta\theta_e$ may also argue these relationships as a possible constraint for downdraft parameterizations.

For the associated precipitation characteristics, these squall-line events exhibit similar total rainfall accumulation (approximately 25 mm, as in Tables S1 and S2) and convective line rainfall (rates to approximately 80 mm/hr, Figure 2c). The more significant discrepancies are found when examining the differences in precipitation contributions from the convective line and trailing stratiform precipitation regions (as designated by RWP observations coupled with the surface instruments). For example, MAO MCSs suggest that the convective line heavily contributes to the total rainfall (i.e., 80%) when compared with data set observations from SGP events (approximately 57%). As discussed by Wang et al. (2018) for Amazon events, we note that our uncertainty in the contribution of convective line precipitation to the total MCS rainfall is approximately 5%, as a fraction of the precipitation has been designated as transitional. These transitional regions include the rearward periphery of the convective lines lacking prominent convective or stratiform radar process signatures in the RWP columns.

When comparing MCS precipitation properties of the Amazon to those of Oklahoma, it is also important to mention the role of baroclinic instability in the formation and evolution of these MCSs. As this forcing is nonexistent in the Amazon, this is one simple explanation as to this particular subset of midlatitude MCSs favoring an enhanced stratiform contribution (i.e., SGP events associated with enhanced background forcing coupled with ice processes favoring additional warming aloft, etc.). Similarly, although we attempt to identify MCS as "mature" in life cycle stage as based on having squall-line features and trailing stratiform shields, we recognize these characteristics as subjective life cycle markers, with the MCS passing over SGP CF typically initiating and/or developing further upwind of their respective site. Moreover, several studies indicate that relative convective and stratiform contributions may vary significantly to within early-mature (updraft dominant) to later-mature (downdraft dominant) stages (e.g., Feng et al., 2018). Finally, manual inspection indicates that RWP column observations do not always generalize MCS precipitation, as this requires assuming steady state life cycle features, as well as favorable symmetry in our trailing-type linear MCS modes (e.g., Parker & Johnson, 2000).

For completeness, one final physical explanation for the differences in the stratiform precipitation contribution is the potential role of wind shear or other environmental factors in MCS organization. For example, weaker wind shear environments at MAO may promote slower convective cells or more upright convective cores less likely to detrain media to developing stratiform regions (e.g., Parker & Johnson, 2000; Romatschke & Houze, 2010; Rotunno et al., 1988). In supporting information Figure S3, we present a scatterplot of the 0- to 5-km wind shear versus the fractional stratiform precipitation for each event. While a positive correlation is found between these quantities ($r \sim 0.5$) across the entire data set, we caution that this correlation is tenuous (Simpson's paradox, e.g., Blyth, 1972), as individual regional positive correlations are substan-

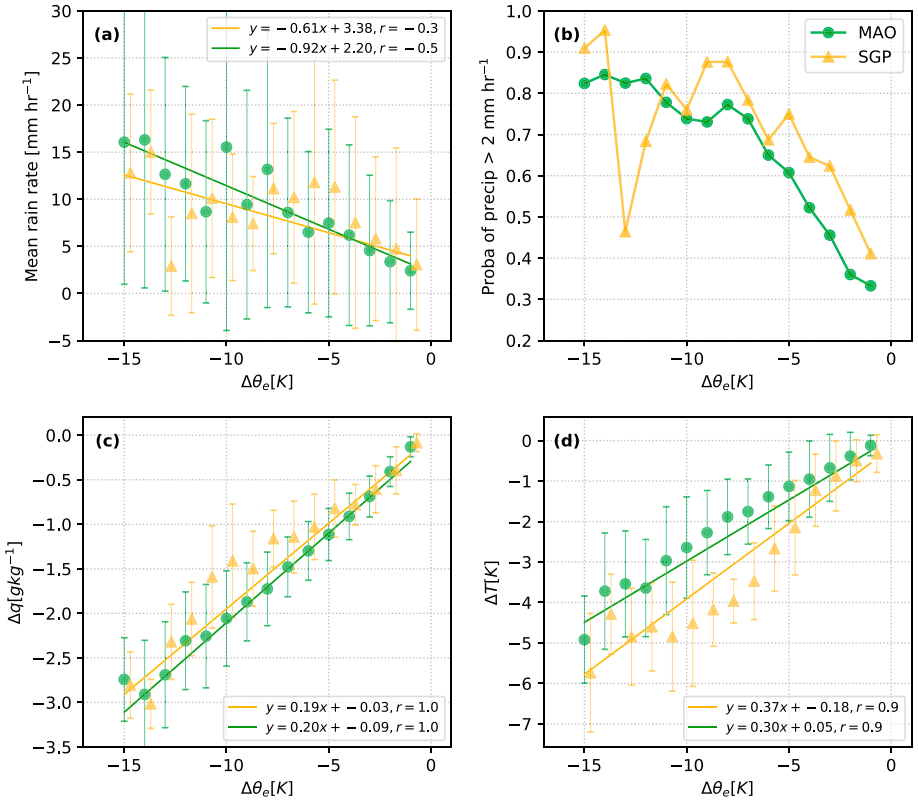

Figure 4. (a) Precipitation rate averaged by coincident changes in equivalent potential temperature ($\Delta\theta_e$) at Amazon (MAO) and Southern Great Plains (SGP) sites (dots). Bins are a width of 1 K, and error bars represent ±1 standard deviation. Solid lines are the linear least squares regression fits. (b) The probability of measurable precipitation ($R > 2$ mm/hr) occurring for a given $\Delta\theta_e$ bin. (c, d) Changes in surface specific humidity (Δq) and temperature (ΔT) as a function of θ_e change ($\Delta\theta_e$).

tially weaker ($r \sim 0.1$). This lack of correlation is not unexpected, especially if considering other potential larger-scale environmental controls. For example, Amazon Dry season events record the lowest total and relative stratiform precipitation contributions. This reduced MCS precipitation may also be consistent with changes in the middle- to upper-level moisture that promote increased evaporation and/or reduction in depositional growth.

3.2. Radar Reflectivity and Vertical Velocity Characteristics

In Figure 5, we plot time-height RWP quantities of the mean radar reflectivity factor (<Z>), the retrieved mean vertical air velocity (<W>), and the 95th percentile vertical velocity. These fields are composited in time-height in a similar manner to surface measurements from Figures 2 and 3. A 2-hr window centered on the maximum R (time = 0) highlights the convective regions where vertical air velocity retrievals are most reliable. Note, composites that account for a radar-based convective line propagating speed have been performed (not shown) but indicate qualitatively similar features as pertaining to the discussions that follow. Note, these images mask out vertical air velocity retrievals in the vicinity of the melting layer due to concerns with the accuracy of the retrieval methods (e.g., Giangrande et al., 2016). Temperatures from radiosonde observations (interpolated in time) have also been overlaid on the upper panels. Additional composites for the Amazon MCSs under Dry, Wet, and Transitional season breakdowns are found in Figure 6.

Structurally, the MAO and SGP MCS events share similarities with an enhanced reflectivity factor (mean exceeding 40 dBZ) near the time of convective line passage as expected given the strong association between Z and R. A characteristic radar bright band (BB) aggregation signature (e.g., Fabry & Zawadzki, 1995) within the trailing stratiform regions is observed close to the 0 °C level for both regions. Reflectivity factor magnitudes to all altitudes within the trailing stratiform region are typically larger for SGP MCS composites, suggesting the more prominent role of depositional growth, aggregation processes, and surface stratiform precipitation as argued previously. Moreover, SGP composites indicate a more intense composite BB signa-

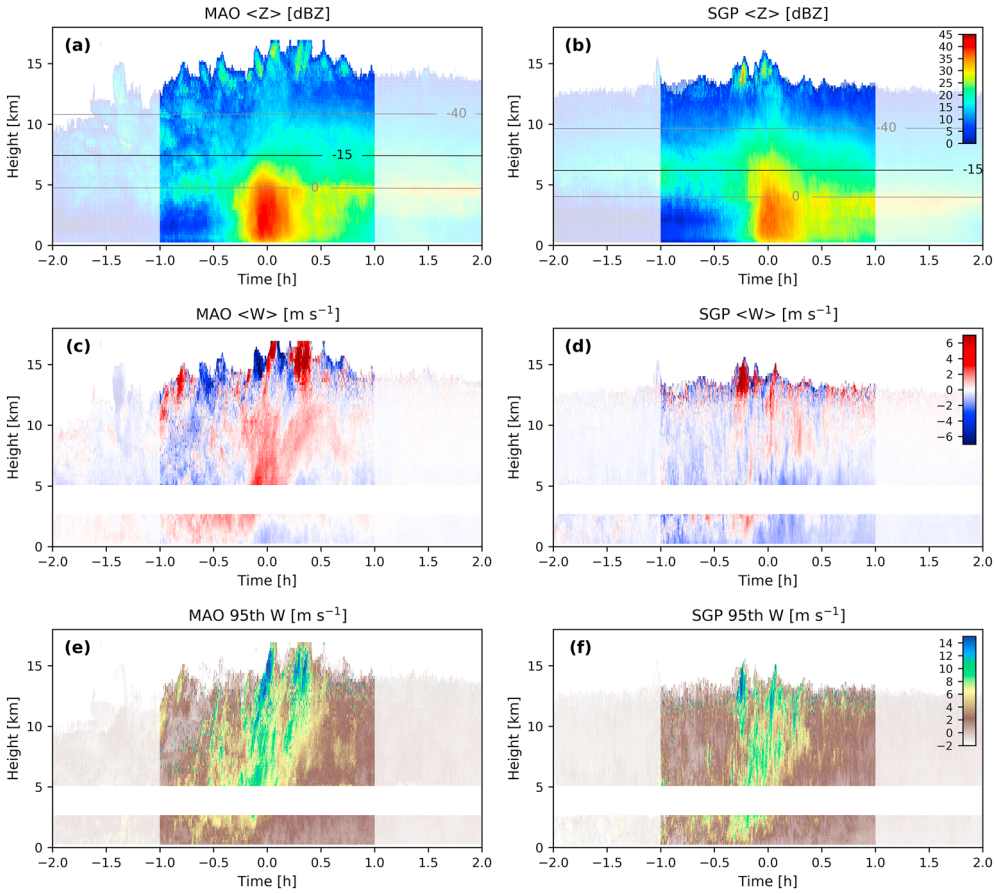

Figure 5. The composite mean radar reflectivity factor (<*Z*>; a, b), mean vertical velocity (<*W*>; c, d), and 95th percentile vertical velocity (e, f) for Amazon (MAO; left panels) and Oklahoma (SGP; right panels) mesoscale convective systems in time-height. A 2-hr window around the maximum rainfall rate (i.e., time 0) has been highlighted. The average temperature profiles (°C) from radiosondes (prior to convective line passage) are overlaid on <*Z*> plots.

ture and *Z* values in the rain regions beneath, in alignment with the expected presence of additional, larger particles, and/or higher stratiform rainfall rates. Signatures of an upper-level leading anvil clouds are also more prominent in the SGP MCS composites. The presence of this anvil clouds is also reflected by the surface radiational cooling trend we observe in composite temperature measurements at SGP (Figures 2a and 2e).

The more intense updrafts are often observed in the middle and upper troposphere and near the time of convective line passage (i.e., time = 0, Figures 5c and 5d). The 95th percentile velocities (Figures 5e and 5f) indicate that the strongest convective air motions accompany line passage and slope rearward in time-height into the stratiform regions. The maximum values for updrafts are typically found at the highest levels (10–15 km) over both regions, well within ice regions. One possible explanation for these intense updraft observations follows from previous arguments regarding the release of latent heat of fusion/freezing of condensate in these regions (e.g., Zipser, 2003). The indication is that the more intense updrafts extend rearward in these composites just prior to the signatures for the onset of aggregation processes and accompanying radar BB signatures beneath. The regions above the melting layers aloft still suggest moderate upward motions consistent with the ideas of the general ascending mesoscale flow and/or decaying cells moving rearward (e.g., Yuter & Houze, 1995a, 1995b). A pronounced precipitation-driven downdraft signature is also consistently found in the composites for both regions, beneath the more intense updraft cores. Strong upper level downdrafts are also observed (as better highlighted in subsequent figures), with SGP MCS events favoring more intense downdrafts over the depth of these MCSs. Similar observations for more intense, nonprecipitation-driven downdrafts to higher altitudes have been previously identified with scanning radars in cumulative velocity coverage profiles by Yuter and Houze (1995b; e.g., their Figure 4) and in profiling radar observations

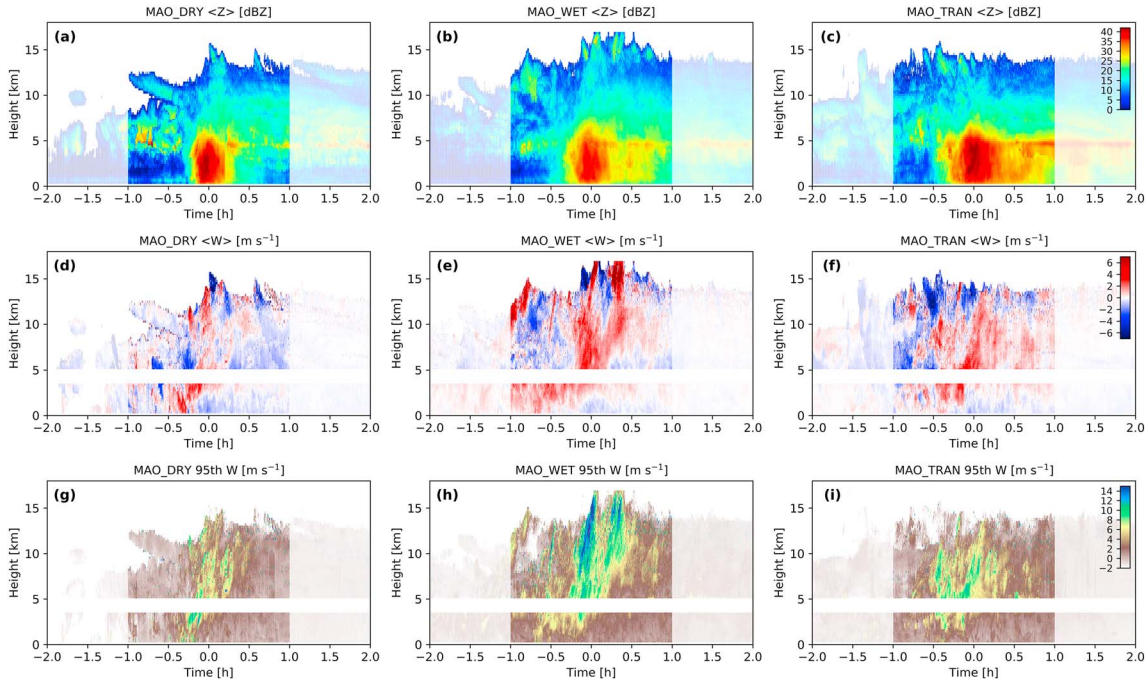

Figure 6. As in Figure 5 but for MAO MCSs during Wet (MAO WET), Dry (MAO DRY) and Transational (MAO TRAN) seasons. MAO = GoAmazon2014/5 campaign; SGP = Southern Great Plains.

(e.g., May & Rajopadhyaya, 1999). To within the stratiform regions beneath the BB, there is also descending motion, as consistent with the ideas for a secondary mesoscale downdraft.

Although these temporal composites are informative, some caution is advised. Event-to-event variability in convective line motion or wind shear conditions will introduce variability in the appearance of upright or sloped updrafts. Since additional storm motion and wind shear variability is observed during SGP MCS events, this acts to smooth SGP composite signatures relative to MAO events around the location of the maximum *R*. As our composite depictions are not steady state, the convective line properties are not those directly associated with the properties of stratiform regions. Nevertheless, this would also be a concern for composites drawn from single time "slices" through an MCS, as stratiform and convective processes operate over different time scales.

For the seasonal breakdowns shown in Figure 6, the Amazon MCS structures are in agreement with previous arguments for surface characteristics shown in Figure 3. As storm motions and wind shear magnitudes are similar across all Amazon events, interpretation for these composite images is more straightforward. Transitional and Wet season precipitation favor more well-developed stratiform regions having larger reflectivity factors. Dry and Transitional season composites suggest larger reflectivity factors in the convective lines, consistent with previous studies that indicate these events as having more intense convective precipitation or updraft properties (e.g., Giangrande et al., 2016; Machado et al., 2004). Wet and Transitional seasons favor more ubiquitous upward motions to most levels and deeper moisture conditions conducive to inflow through a deep lower tropospheric layer (e.g., Schiro & Neelin, 2018). The Dry season indicates more intense and more frequent downdraft signatures, consistent with drier midlevel humidity conditions promoting additional evaporative cooling and therefore more intense downdrafts to higher altitudes.

4. Composite MCS Updraft and Downdraft Statistics

4.1. Updraft, Downdraft, and Mass Transport Profiles

In Figure 7a, we plot the data set mean, 5th and 95th percentile values for the vertical velocity profiles as observed within the convective line regions for MCS events. Qualitatively, these profiles are consistent with deep convective vertical velocity profiles found in previous RWP studies for these locations (e.g., Giangrande et al., 2013, 2016). For these events, the mean *W* profile during MAO MCSs is dominated by updrafts (2–12 km), whereas for SGP MCSs, the mean vertical air motion is negligible and/or skewed toward downward motions at lower altitudes. The 5th and 95th percentiles of *W* suggest similar magnitudes for the statistical

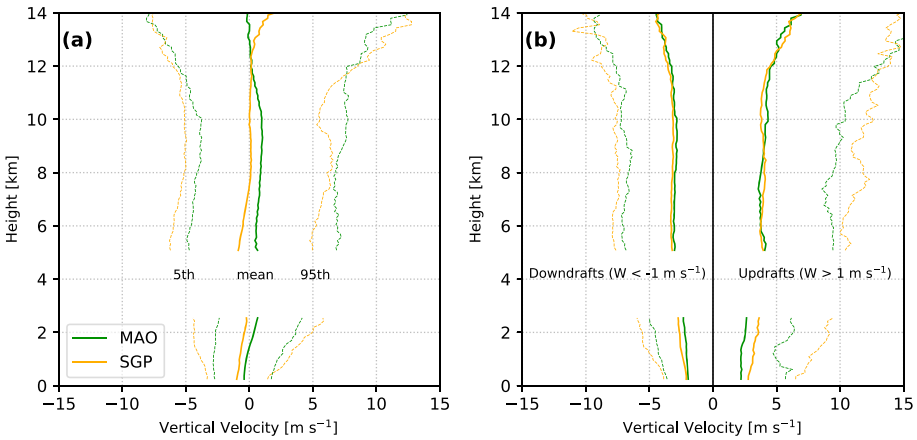

Figure 7. (a) Mean (solid line) and 5th and 95th (dotted lines) vertical velocity profiles for Oklahoma (SGP) and Amazon (MAO) mesoscale convective system events within convective line regions. (b) Vertical velocity profiles for more significant SGP and MAO mesoscale convective system downdrafts ($W < -1$ m/s; left side) and updrafts ($W < 1$ m/s; right side).

vertical air velocity properties within MCSs. In following the discussions from the previous section, mean vertical air velocity profiles may also be influenced by the frequency and/or magnitudes of updrafts and downdrafts sampled. In this regard, these profiles may be influenced by disproportionate samples (in terms of poor event selection or representativeness of updraft/downdraft fraction therein).

To vary our characterization of MCS vertical motions, we also plot the mean and 95th/5th percentile updraft ($W > 1$ m/s) and downdraft ($W > -1$ m/s) profiles in Figure 7b. The two locations retain a similar vertical velocity profile shape. However, vertical air motions within SGP MCSs are typically more intense in terms of mean and percentile behaviors when conditionally sampled to updraft/downdraft regions. For all velocity observations in Figure 7, the number of valid observations decreases with altitude. Thus, the strongest/deepest convective cells will exclusively dominate these profile behaviors, whereas lower altitudes carry contributions from all cloud depths.

To better account for variations in convective cloud depth, we sort RWP observations based on the radar echo top height (ETH). In Figure 8, we plot the mean, 95th-, and 5th-percentile convective vertical velocity profiles according to convective ETH in 1-km bin increments. For these plots, the ETH is defined as the altitude where Z in the clouds drops below 10 dBZ. Based on initial inspection of Figure 8, this relative 10-dBZ value is also a reasonable approximation for cloud top height since the mean vertical air velocity profiles approach 0 m/s along the one-to-one line between ETH and height above the ground. The gray lines overlaid on Figure 8 indicate the number of samples for each ETH increment. A similar set of plots for MAO seasonal breakdowns is provided for additional reference in Figure S4. Mean profiles of mass transport as a function of ETH are obtained by weighting the measured vertical air velocities by the air density (as based on nearby radiosonde profiles for each event) but mirrors the profiles of the vertical velocity (see Figure S5). The difference between MAO and SGP mean mass transportation profiles is provided in Figure S6. This suggests larger upward and downward mass transport for SGP MCSs to within the deeper ETH convective regions.

The ETH sorting approach for profiling helps to highlight several structural differences between the velocity properties of the two MCS regimes. Within the deeper parts of the convective lines, larger mean, and 95th-percentile updrafts are observed, and mean updraft properties are found to increase in magnitude with height. Peak updraft velocities (95th percentiles) are observed at approximately 10 and 12 km for MAO and SGP, respectively (Figures 8b and 8e). The mean and 95th percentile upward motions are significantly weaker within the deeper portions of the MAO MCSs. The MAO mean profiles are more dominated by updrafts than SGP profiles (e.g., Figures 8a and 8c), with MAO mean downdraft profile signatures weaker and concentrated well below the ambient freezing level. The low-level air motions and upward and downward mass transport for MAO MCSs are similar in magnitude even to these mature stages (Figure S5), suggesting negligible net mass flux at low levels consistent with several previous studies (e.g., Frank & McBride, 1989; LeMone & Zipser, 1980; Lucas et al., 1994; May & Rajopadhyaya, 1996). However, SGP mean

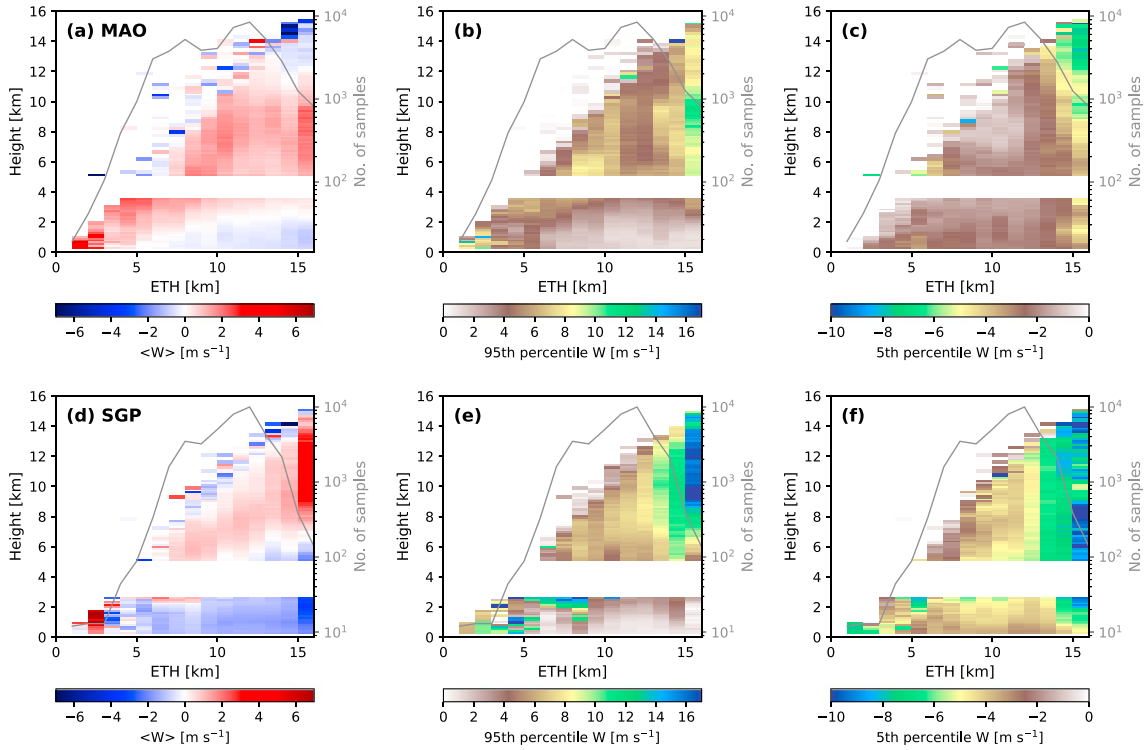

Figure 8. Mean (a, d), 95th (b, e), and 5th (c, f) vertical velocity profiles as sorted by radar echo top height (ETH; 10 dBZ) for Amazon (MAO; top) and Oklahoma (SGP; bottom) mesoscale convective systems. As in Figure 7, only convective line regions are considered. The gray lines report the number of profiles.

and 95th vertical velocity profiles indicate more intense updrafts, peaking at higher altitudes. Figure 8 also suggests the more prominent role of downdrafts at all altitudes within SGP MCS convective regions. This includes larger mean downward profile values concentrated in the lower 6 km, as well as larger 5th percentile maximum downward velocities observed at all altitudes in higher ETH parts of the convective lines (Figure 8f). Nevertheless, a secondary peak in downdraft frequency and intensity at higher altitudes (non-precipitation driven) is also observed at MAO as previously suggested by Yuter and Houze (1995b). Seasonal MAO variability, as shown in supporting information Figure S4, is noisy and possibly reflects some limitations for our Amazon RWP sampling. However, the profiles are consistent with the Dry and Transitional seasons favoring the larger mean and maximum profile updrafts, and the Dry season favoring deeper and more intense mean profile downdraft signatures.

Overall, combining the information from Figures 5 and 8, the vertical velocity characteristics at MAO suggest the consistent presence of upward air motions from the surface to upper levels associated with convective line passages. In this way, MAO events favor more ubiquitous but weaker mean and maximum upward motions and fewer downdrafts (with bimodality for lower and upper levels). In contrast, SGP events record the stronger updrafts and downdrafts (magnitudes and mean profile values), as well as the more prominent precipitation-driven downdrafts. We also observe an increased downdraft frequency and stronger downdraft intensities to most altitudes. Therefore, while Amazon composites in Figure 5 indicate updrafts as prominent features, those higher composite values simply suggest that there is less variability in the presence of MAO updrafts around the time of maximum R. Similarly, the dominant downdraft signatures at SGP and absence of a persistent updraft feature reflects on downdraft frequency and intensity for the regions adjacent to that maximum R.

While larger MUCAPE values are consistently observed for MAO events (Table S1 and composite radiosonde in Figure 1), the SGP MCS environments are associated with larger MUCIN values and steeper ELRs. The combination of (i) enhanced background (frontal) forcing, (ii) capped (high-CIN) environments aiding in the development of an unstable air mass during the hours prior to convective triggering, and (iii) these steeper lapse rates for SGP events likely explains the updrafts we observe and the lack of correlation with the MUCAPE parameter. Higher wind shear for SGP events may also promote sloped (less upright) updrafts that

could reduce the role of precipitation drag that may impede storm updrafts. As before, larger magnitudes for air motions aloft in the 10- to 15-km range may also follow from the release of latent heat of fusion/freezing of condensate in these regions (e.g., Zipser, 2003). The precipitation-driven downdrafts and intercomparison between Amazon and Oklahoma will be further discussed in subsequent sections. However, we will note that both the SGP and the Amazon Dry season favor drier midlevels, which likely contributes to enhanced downward vertical air motions and potentially more intense cold pools (through evaporative cooling).

4.2. Updraft and Downdraft Probability

As first suggested by Schiro and Neelin (2018), the probability of observing updrafts and downdrafts within RWP columns as a function of radar reflectivity is plotted (Figure 9). These plots align with previous statements on updraft/downdraft frequency and provide a simple reference that couples dynamic and microphysical quantities typically available from cloud-resolving models with forward radar operators. As with velocity profiles, these probability charts reflect properties from convective line regions as designated by echo classification. Dashed lines on the plots indicate the number of samples within each Z bin. The solid lines indicate the likelihood to observe any instance of vertical air motions in the column exceeding 1, 3, and 5 m/s, respectively.

At lower altitudes (2-km altitude, Figure 9a), weaker precipitation regions (i.e., $Z < 35$ dBZ) indicate a small percentage of columns have instances of upward vertical air motion. The probability to observe convective air motions $W > 3$ m/s is negligible for weaker values of Z typically located near the periphery of the convective lines. As Z increases into higher precipitation regions, the likelihood for sampling a convective updraft in the column also increases. This low-level relationship between Z and convective updraft probability holds across both regions. The likelihood to observe an upward motion $W > 3$–5 m/s within intense convective regions ($Z > 50$ dBZ and/or approximately 80 mm/hr) is below 30%, although half of these intense convective columns record an instance of $W > 1$ m/s.

The probability of observing downdrafts is less dependent on the lower-level Z (proxy for precipitation rate), with higher Z values typically weakly associated with a higher chance to observe an intense downdraft (Figure 9c). The low-level results generally align with those from Figure 4 that suggest the colder cold pools are those associated with the higher rainfall rate (or Z) regions. The most striking difference in downdraft behaviors is an overall increase in frequency of significant downdraft observations at SGP, in alignment with previous mean profile and composite expectations. The likelihood to observe a lower-level downdraft at SGP is approximately double that at MAO and persistent for all relative Z (precipitation) conditions. Overall, the probabilities for observing significant downdrafts $W < -3$ m/s in the most intense portions of the convective lines (e.g., $Z \sim 50$ dBZ, approximately 10–20% columns having downdrafts) are lower than those for updrafts (approximately 30%), with downdrafts typically more common than updrafts in the lower-level periphery ($Z < 35$ dBZ) convective precipitation regions.

For higher altitude updraft behaviors (6-km altitude, Figures 9b and 9d), we still observe an increasing likelihood to observe a more intense vertical air velocity to higher Z values. These bulk probabilities have shifted higher, which is anticipated since a similar Z intensity at a higher altitude argues for a stronger storm (e.g., Zipser & Lutz, 1994). Amazon MCSs suggest a higher likelihood to record upward motion $W > 3$ m/s for the same relative Z value as SGP. Physically, this should also be anticipated since these storms are required under bulk Amazon thermodynamics conditions to achieve similar Z magnitudes to similar altitudes, based on propensity for graupel and/or hail production. As with downdraft properties and their relationship to lower-level Z, there is a slight enhancement in downdraft frequency for storms with elevated reflectivities (e.g., having $Z > 30$ dBZ) in convective regions. Nevertheless, the probability for observing significant downdrafts $W < -3$ m/s is typically below 20%. As before, the relative increase in downdrafts we observe with increasing Z is associated with those columns having intense convective precipitation cores. Unlike the Z properties at 2 km, we find that the probability of pinpointing columns with vertical motions $W > 3$ m/s is more successful at 6 km, speaking to the improved success in relating convective updraft intensity to integrated column Z measurements (e.g., Zipser & Lutz, 1994). Similar probability calculations have been performed on two temperature levels (15 and −10 °C) for both sites (not shown). Overall, the updraft and downdraft behaviors are very similar as reported in Figure 9.

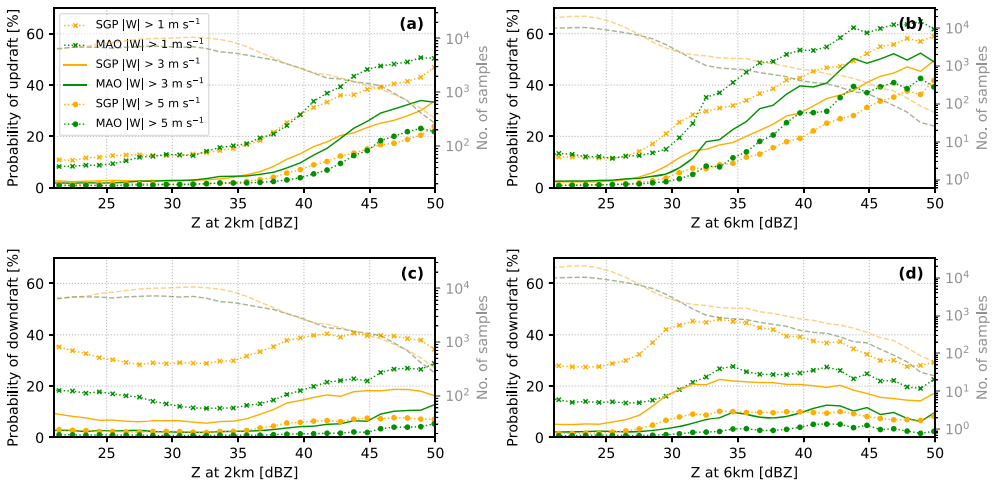

Figure 9. The probability of observing an updraft or downdraft within an radar wind profiler column ($|W| > 1$ m/s / 3 m/s / 5 m/s) for a given radar reflectivity magnitude at 2 km (a, c) and 6 km (b, d). The number of samples are plotted as dashed lines. MAO = GoAmazon2014/5 campaign; SGP = Southern Great Plains.

5. Mixing and Source of Downdraft Air

Although convective precipitation rates and associated cold pools share several aspects in our bulk MCS depictions, one key discrepancy between MAO and SGP events is the change in the frequency, vertical extent, and intensity of downdrafts. To investigate the downdraft origin heights and associated properties, many methods have been suggested (e.g., Betts, 1976; Betts & Silva Dias, 1979; Betts & Jakob, 2002; Brancato, 1942; Fawbush & Miller, 1954; Foster, 1958; Rasmussen et al., 1994; Schiro & Neelin, 2018; Zipser, 1969). In this study, θ_e is used as a tracer, since it is nearly conserved for both dry and moist adiabatic processes (no mass and energy is exchanged with the environment). As an initial approach, we assume that no mixing occurs between the air parcel and the environmental air and that the downdraft originates from a single level. Here tracing the surface θ_e within MCS cold pools to the corresponding value aloft as obtained from radiosondes may serve as one reference for an initial downdraft level. However, air parcels of lower θ_e transported through downdrafts are likely diluted by high θ_e environment air from the boundary layer through turbulent mixing (e.g., Schiro & Neelin, 2018). Thus, downdraft air parcels ending with the same surface θ_e may originate from multiple heights. Therefore, our MCS radiosonde analysis will also consider the potential mixing associated with downdrafts.

Composite behaviors for the probability of observing downdrafts ($W > -1$ m/s) and updrafts ($W > 1$ m/s) for selected MAO and SGP MCSs are plotted in Figure 10. Low-level downdrafts are predominantly associated with deep convective clouds and coincident with the maximum convective rainfall rate. There is a higher probability to observe significant downdrafts for SGP MCSs, as also suggested from previous depictions in Figure 9. The SGP events also suggest a higher probability to observe significant downdrafts over a greater atmospheric depth (to 6 km) when compared to Amazon events (e.g., Figures 11a and 11b). For updraft properties, the patterns are qualitatively similar, with the highest probability to observe a significant updraft $W > 1$ m/s typically located to with 30 min of the maximum rainfall rate (Figures 11c and 11d).

In order to assess the nature of mixing that could be occurring between the downdrafts and their surrounding environments, a range of assumptions is tested in Figure 11. We first average θ_e profiles as estimated from the closest radiosondes (as listed in supporting information Tables S1 and S2) prior to convective line passage over RWP locations to best approximate prestorm MCS environments for these events. Since the diurnal behavior for MCS events was not always similar, the averaged θ_e profiles derived from radiosondes launched at different launch times are also overlaid as reference to this. As from previous sections, low levels are cooled after convective line passage, which leads to a substantial θ_e drop at the surface of approximately 10 K for these SGP and MAO events (e.g., Figure 2a).

Potential origin heights of downdrafts are examined by assuming different bulk mixing rates (constant with height), calculated following methods in Schiro and Neelin (2018). First, we consider a case in which downdrafts travel undiluted to the surface, conserving θ_e. For this analysis, we subtract 10 K from the mean surface

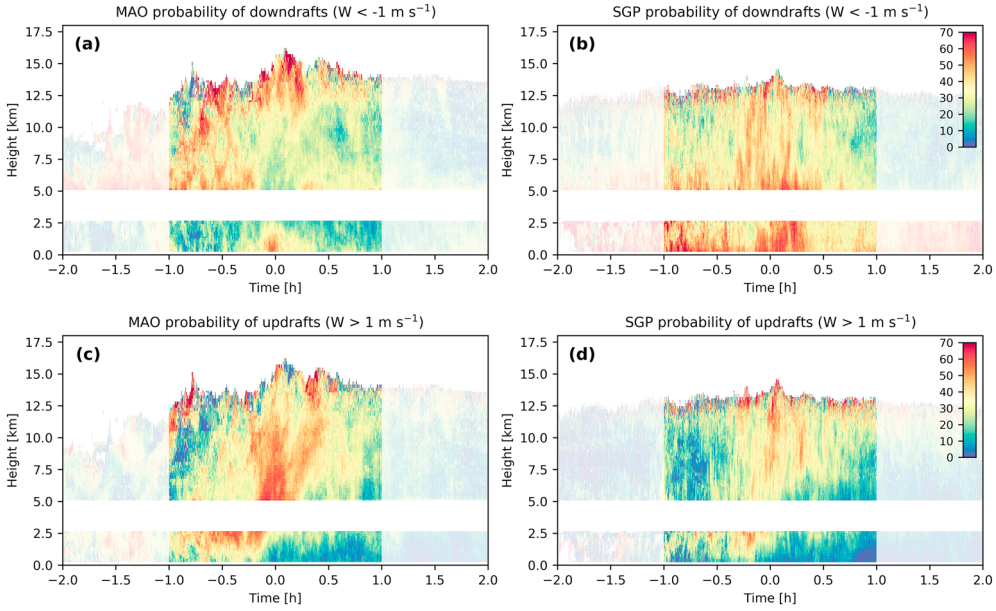

Figure 10. As in Figure 5, the probability of observing downdrafts (a, b) and updrafts (c, d) greater than 1 m/s, for Amazon (MAO) and Oklahoma (SGP) mesoscale convective systems in time-height.

θ_e value ($\theta_{e,sfc}$) from the radiosonde profile and determine the height at which $\theta_{e,sfc}$—10 K is observed in the profile. The height of the crossing point for this line with the sounding θ_e profile is assumed as the initial altitude of an unmixed downdraft parcel. These values are approximately 2.4 km for MAO (similar to that reported in Schiro & Neelin, 2018) and 2.8 km for SGP. Thus, it is likely that MCS downdrafts are originating at higher altitudes in both regions, on average, if mixing occurs between the downdrafts and their environments.

For both MAO and SGP events, if assuming a constant linear mixing rate (χ) of 0.1 km^{-1}, the origin height of air parcels descending to the surface increases to approximately 2.8–3 km. This is illustrated by the dashed red lines on plots in Figure 11. Parcels descending to the surface from a height of 4 km would have experienced a larger mixing rate, $\chi = 0.24$ km^{-1} for SGP and $\chi = 0.17$ km^{-1} for MAO. For the SGP events, the environment is drier aloft at midlevels, and the level of minimum θ_e is approximately 6 km. Since SGP MCSs originate within and ingest drier air, this potentially aids in the development of downdrafts. The θ_e

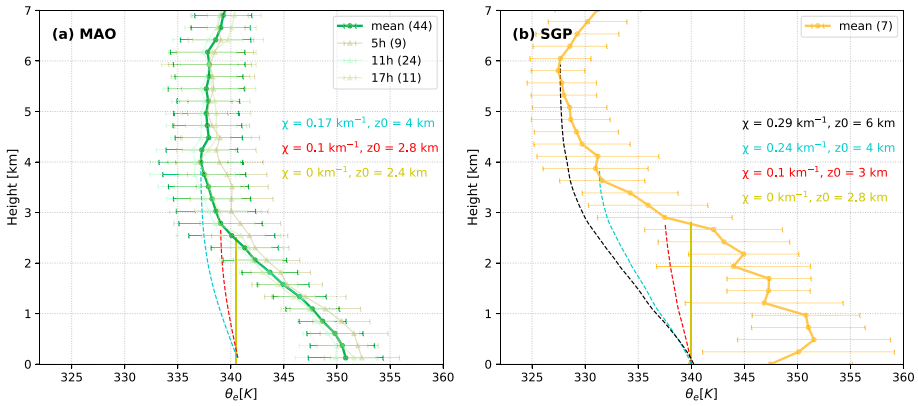

Figure 11. Mean profiles of θ_e (thick solid lines) from radiosondes launched prior to convective lines for Amazon (MAO; 44 profiles) and Oklahoma (SGP; 7 profiles launched around 5:30 hr) mesoscale convective systems. Profiles are grouped according to the launch time. Mean profile behaviors for each time have been plotted as thin solid lines. Dashed red and light blue lines indicate the mean descent path for air parcels originating at various altitudes mixing with the environment at corresponding rates. The solid yellow lines report mean descent without mixing. Error bars reflect ±1 standard deviation values.

difference between the surface and the minimum level of θ_e for SGP MCSs (approximately 23 K) is larger than for MCSs at MAO (approximately 14 K); however, the vertical gradient in the lower troposphere is relatively consistent across sites, resulting in similar mixing rates for downdrafts originating below ~4 km. If downdrafts originate nearer to the level of minimum θ_e at SGP, it is likely that mixing is occurring at rates comparable to $\chi = 0.29\ \mathrm{km}^{-1}$. We note, however, that these are simplified mixing assumptions; we test such assumptions to inform decisions about interactions between downdrafts and their environments in GCMs, though we note that downdrafts need not be considered as a single plume descending toward the surface and mixing turbulently with the surrounding environment.

6. Summary

This study contrasts the characteristics of mature stage continental MCS events as collected by ARM RWP deployments for multiyear periods over tropical Amazon and midlatitude Oklahoma. The associated precipitation, cold pool, and dynamical characteristics have been evaluated to better quantify the kinematic structure and precipitation variability associated with MCSs and larger-scale environmental shifts therein. The effort also includes analyses to determine the possible origin heights of MCS downdrafts, with downdraft likelihood and intensity identified as a key discrepancy in the observed differences between these regions. Although the RWP observations and extremes reflect vertical velocity observations to scales $O(<1$ km), the mean and tail convective profile characteristics, probabilities, and downdraft mixing analyses have potential usefulness for improving MCS representations to coarser model scales. For example, several climate models (including the European Centre for Medium-Range Weather Forecasts Integrated Forecasting System and the Goddard Institute for Space Studies Model E2 GCM) assume constant mixing rate values (e.g., $\chi = 0.2\ \mathrm{km}^{-1}$). As suggested by our simple MCS analyses, if downdrafts originate nearer to the level of minimum θ_e at SGP, it is likely that mixing is occurring at rates comparable to $\chi = 0.3\ \mathrm{km}^{-1}$.

Overall, the key findings of this study are summarized as follows:

- The continental tropical and midlatitude MCS events in our data set share several mean properties of their convective lines, including rainfall rate intensity, total convective rainfall, and associated surface thermodynamic shifts within the convective cold pools. The primary precipitation change is in the fractional stratiform precipitation contribution to the total rainfall accumulation. SGP events suggest larger stratiform contributions when compared to MAO counterparts, attributed to the difference in background baroclinic forcing and/or additional life cycle sampling considerations associated with the regional data sets.
- The properties of the convective cold pools were observed to be similar for MAO and SGP events, typically associated with a 10-K drop in the surface θ_e near convective line passage. The θ_e drop demonstrates a modest correlation with the surface rainfall rate and the propensity to observe measurable precipitation. These behaviors are similar for both MCS locations. There is indication that cold pools from SGP events are associated with higher surface pressure increases and reduced temperatures, suggesting those cold pools as stronger for similar surface rainfall. This result is consistent with the expectation for additional evaporative cooling for drier thermodynamic profiles.
- Mean vertical velocity and mass transport profiles are constructed. Specific emphasis is placed on mean velocity profiles as a function of ETH and for more significant updrafts and downdrafts ($|W| > 1$ m/s). Mean profile shapes and magnitudes are initially similar when considering statistical properties from all MCS convective lines. However, when accounting for only significant vertical velocity regions ($|W| > 1$ m/s) or ETH variability, SGP profiles indicate more intense vertical motions with updraft magnitudes peaking to higher altitudes. Mass transport profiles are similar to the vertical velocity profiles. The Amazon MCS preferentially favor weaker, but mostly upward motions to most altitudes. These findings are consistent with enhanced background forcing and greater instability for SGP events.
- There is a much higher propensity for downdrafts in Oklahoma and Amazon Dry season events, including precipitation-driven downdrafts originating near higher altitudes (6 km) in SGP composites. In addition, convective downdrafts are more intense and more frequent to all altitudes at SGP when compared to MAO MCS events. The latter is suggested as consistent with SGP background forcing, ELRs, "fatter" CAPE in the lower to midlevels, and higher CIN values conducive to more intense convective air motions (e.g., Lucas et al., 1994; Lucas et al., 1994). A simple radiosonde-based analysis is performed to better inform modelers on downdraft representation. For these MCS cases, similar mixing rates for downdrafts originating below 3 km ($\chi \sim 0.1\ \mathrm{km}^{-1}$) are suggested. For the SGP observations that suggest downdrafts may originate nearer

to the level of minimum θ_e (approximately 6 km), mixing may be occurring at rates close to $\chi = 0.3\ \mathrm{km}^{-1}$. Both SGP and MAO convective lines are characterized by upper-level downdrafts responding to buoyancy pressure gradient forces as described by Yuter and Houze (1995b).

Acknowledgments
This study was supported by the U.S. Department of Energy (DOE) Atmospheric System Research (ASR) Program and the Climate Model Development and Validation (CMDV) program. This paper has been authored by employees of Brookhaven Science Associates, LLC, under contract DE-SC0012704 with the U.S. DOE. The publisher by accepting the paper for publication acknowledges that the United States Government retains a nonexclusive, paid-up, irrevocable, worldwide license to publish or reproduce the published form of this paper, or allow others to do so, for United States Government purposes. The Pacific Northwest National Laboratory (PNNL) is operated for the DOE by Battelle Memorial Institute under contract DE-AC06-76RLO1830. We also acknowledge the Atmospheric Radiation Measurement (ARM) program, a user facility of the U.S. DOE, Office of Science, sponsored by the Office of Biological and Environmental Research, and support from the ASR program of that office. All ARM data sets used for this study (at SGP site and during GoAmazon2014/5 field campaign) can be downloaded at http://www.arm.gov and associated with several "value added product" streams.

References

Atlas, D., Williams, C. R., & 3–15 (2003). The anatomy of a continental tropical convective storm. *Journal of the Atmospheric Sciences*, *60*(1). https://doi.org/10.1175/1520-0469(2003)060h0003:TAOACTi2.0.CO;2

Augustine, J. A., & Zipser, E. J. (1987). The use of wind profilers in a mesoscale experiment. *Bulletin of the American Meteorological Society*, *68*(1), 4–17. https://doi.org/10.1175/1520-0477(1987)068h0004:TUOWPIi2.0.CO;2

Barnes, H. C., & Houze Jr., R. A. (2016). Comparison of observed and simulated spatial patterns of ice microphysical processes in tropical oceanic mesoscale convective systems. *Journal of Geophysical Research: Atmospheres*, *121*, 8269–8296. https://doi.org/10.1002/2016JD025074

Betts, A. K. (1976). The thermodynamic transformation of the tropical subcloud layer by precipitation and downdrafts. *Journal of the Atmospheric Sciences*, *33*(6), 1008–1020. https://doi.org/10.1175/1520-0469(1976)033h1008:TTTOTTi2.0.CO;2

Betts, A. K., & Jakob, C. (2002). Study of diurnal cycle of convective precipitation over Amazonia using a single column model. *Journal of Geophysical Research*, *107*(D23), 4732. https://doi.org/10.1029/2002JD002264

Betts, A. K., & Silva Dias, M. F. (1979). Unsaturated downdraft thermodynamics in cumulonimbus. *Journal of the Atmospheric Sciences*, *36*(6), 1061–1071. https://doi.org/10.1175/1520-0469(1979)036h1061:UDTICi2.0.CO;2

Biggerstaff, M. I., & Houze, R. A. (1991). Kinematic and precipitation structure of the 10–11 June 1985 squall line. *Monthly Weather Review*, *119*(12), 3034–3065. https://doi.org/10.1175/1520-0493(1991)119h3034:KAPSOTi2.0.CO;2

Blyth, C. R. (1972). On Simpson's paradox and the sure-thing principle. *Journal of the American Statistical Association*, *67*(338), 364–366.

Bolton, D. (1980). The computation of equivalent potential temperature. *Monthly Weather Review*, *108*(7), 1046–1053. https://doi.org/10.1175/1520-0493(1980)108h1046:TCOEPTi2.0.CO;2

Brancato, G. N. (1942). The meteorological behavior and characteristics of thunderstorms. Hydrometeorological Tech. Paper , 3 , 22.

Bretherton, C. S., & Khairoutdinov, M. F. (2015). Convective self-aggregation feedbacks in near-global cloud-resolving simulations of an aquaplanet. *Journal of Advances in Modeling Earth Systems*, *7*, 1765–1787. https://doi.org/10.1002/2015MS000499

Byers, H. R., & Braham, R. R. (1948). Thunderstorm structure and circulation. *Journal of Meteorology*, *5*(3), 71–86. https://doi.org/10.1175/1520-0469(1948)005h0071:TSACi2.0.CO;2

Cifelli, R., Carey, L., Petersen, W. A., & Rutledge, S. A. (2004). An ensemble study of wet season convection in southwest Amazonia: Kinematics and implications for diabatic heating. *Journal of Climate*, *17*(24), 4692–4707. https://doi.org/10.1175/JCLI-3236.1

Cifelli, R., Petersen, W. A., Carey, L. D., Rutledge, S. A., & da Silva Dias, M. A. F. (2002). Radar observations of the kinematic, microphysical, and precipitation characteristics of two MCSs in TRMM LBA. *Journal of Geophysical Research*, *107*(D20), 8077. https://doi.org/10.1029/2000JD000264

Cifelli, R., & Rutledge, S. A. (1994). Vertical motion structure in maritime continent mesoscale convective systems: Results from a 50-MHz profiler. *Journal of the Atmospheric Sciences*, *51*(18), 2631–2652. https://doi.org/10.1175/1520-0469(1994)051h2631:VMSIMCi2.0.CO;2

Cifelli, R., & Rutledge, S. A. (1998). Vertical motion, diabatic heating, and rainfall characteristics in north Australia Convective Systems. *Quarterly Journal of the Royal Meteorological Society*, *124*(548), 1133–1162. https://doi.org/10.1002/qj.49712454806

Collis, S., Protat, A., May, P. T., & Williams, C. (2013). Statistics of storm updraft velocities from TWP-ICE including verification with profiling measurements. *Journal of Applied Meteorology and Climatology*, *52*(8), 1909–1922. https://doi.org/10.1175/JAMC-D-12-0230.1

Del Genio, A. D., Chen, Y., Kim, D., & Yao, M.-S. (2012). The MJO transition from shallow to deep convection in CloudSat/CALIPSO data and GISS GCM simulations. *Journal of Climate*, *25*(11), 3755–3770. https://doi.org/10.1175/JCLI-D-11-00384.1

Del Genio, A. D., & Kovari, W. (2002). Climatic properties of tropical precipitating convection under varying environmental conditions. *Journal of Climate*, *15*(18), 2597–2615. https://doi.org/10.1175/1520-0442(2002)015h2597:CPOTPCi2.0.CO;2

Del Genio, A. D., Wu, J., & Chen, Y. (2012). Characteristics of mesoscale organization in WRF simulations of convection during TWP-ICE. *Journal of Climate*, *25*(17), 5666–5688. https://doi.org/10.1175/JCLI-D-11-00422.1

Donner, L. J. (1993). A cumulus parameterization including mass fluxes, vertical momentum dynamics, and mesoscale effects. *Journal of the Atmospheric Sciences*, *50*(6), 889–906. https://doi.org/10.1175/1520-0469(1993)050h0889:ACPIMFi2.0.CO;2

Donner, L. J., O'Brien, T. A., Rieger, D., Vogel, B., & Cooke, W. F. (2016). Are atmospheric updrafts a key to unlocking climate forcing and sensitivity? *Atmospheric Chemistry and Physics*, *16*(20), 12,983–12,992. https://doi.org/10.5194/acp-16-12983-2016

Donner, L. J., Seman, C. J., Hemler, R. S., & Fan, S. (2001). A cumulus parameterization including mass fluxes, convective vertical velocities, and mesoscale effects: Thermodynamic and hydrological aspects in a general circulation model. *Journal of Climate*, *14*(16), 3444–3463. https://doi.org/10.1175/1520-0442(2001)014h3444:ACPIMFi2.0.CO;2

Engerer, N. A., Stensrud, D. J., & Coniglio, M. C. (2008). Surface characteristics of observed cold pools. *Monthly Weather Review*, *136*, 4839–4849. https://doi.org/10.1175/2008MWR2528.1

Fabry, F., & Zawadzki, I. (1995). Long-term radar observations of the melting layer of precipitation and their interpretation. *Journal of the Atmospheric Sciences*, *52*(7), 838–851. https://doi.org/10.1175/1520-0469(1995)052h0838:LTROOTi2.0.CO;2

Fan, J., Han, B., Varble, A., Morrison, H., North, K., Kollias, P., et al. (2017). Cloud-resolving model intercomparison of an MC3E squall line case: Part I—Convective updrafts. *Journal of Geophysical Research: Atmospheres*, *122*, 9351–9378. https://doi.org/10.1002/2017JD026622

Fawbush, E. J., & Miller, R. C. (1954). A basis for forecasting peak wind gusts in non-frontal thunderstorms. *Bulletin of the American Meteorological Society*, *35*(1), 14–19. http://www.jstor.org/stable/26242388

Feng, Z., Leung, L. R., Hagos, S., Houze, R. A., Burleyson, C. D., & Balaguru, K. (2016). More frequent intense and long-lived storms dominate the springtime trend in central US rainfall. *Nature Communications*, *7*, 13429. https://doi.org/10.1038/ncomms13429

Feng, Z., Leung, L. R., Houze, R. A., Hagos, S., Hardin, J., Yang, Q., et al. (2018). Structure and evolution of mesoscale convective systems: Sensitivity to cloud microphysics in convection-permitting simulations over the United States. *Journal of Advances in Modeling Earth Systems*, *10*, 1470–1494. https://doi.org/10.1029/2018MS001305

Foster, D. S. (1958). Thunderstorm gusts compared with computed downdraft speeds. *Monthly Weather Review*, *86*(3), 91–94. https://doi.org/10.1175/1520-0493(1958)086h0091:TGCWCDi2.0.CO;2

Frank, W. M., & McBride, J. L. (1989). The vertical distribution of heating in AMEX and GATE cloud clusters. *Journal of the Atmospheric Sciences*, *46*(22), 3464–3478. https://doi.org/10.1175/1520-0469(1989)046h3464:TVDOHIi2.0.CO;2

Fritsch, J. M., Kane, R. J., & Chelius, C. R. (1986). The contribution of mesoscale convective weather systems to the warm-season precipitation in the United States. *Journal of Climate and Applied Meteorology*, *25*(10), 1333–1345. https://doi.org/10.1175/1520-0450(1986)025h1333:TCOMCWi2.0.CO;2

Fujita, T. (1963). Analytical mesometeorology: A review. In *Severe local storms, Meteorological monographs* (Vol. 5, pp. 77–125). Boston, MA: American Meteorological Society.

Gettelman, A., & Sherwood, S. C. (2016). Processes responsible for cloud feedback. *Current Climate Change Reports*, *2*(4), 179–189 English. This article is part of the Topical Collection on Climate Feedbackshttps://doi.org/10.1007/s40641-016-0052-8

Giangrande, S. E., Collis, S., Straka, J., Protat, A., Williams, C., & Krueger, S. (2013). A summary of convective-core vertical velocity properties using ARM UHF wind profilers in Oklahoma. *Journal of Applied Meteorology and Climatology*, *52*(10), 2278–2295. https://doi.org/10.1175/JAMC-D-12-0185.1

Giangrande, S. E., Feng, Z., Jensen, M. P., Comstock, J. M., Johnson, K. L., Toto, T., et al. (2017). Cloud characteristics, thermodynamic controls and radiative impacts during the Observations and Modeling of the Green Ocean Amazon (GoAmazon2014/5) experiment. *Atmospheric Chemistry and Physics*, *17*(23), 14,519–14,541. https://doi.org/10.5194/acp-17-14519-2017

Giangrande, S. E., Toto, T., Jensen, M. P., Bartholomew, M. J., Feng, Z., Protat, A., et al. (2016). Convective cloud vertical velocity and mass-flux characteristics from radar wind profiler observations during GoAmazon2014/5. *Journal of Geophysical Research: Atmospheres*, *121*, 12,891–12,913. https://doi.org/10.1002/2016JD025303

Hartmann, D. L., Hendon, H. H., & Houze, R. A. (1984). Some implications of the mesoscale circulations in tropical cloud clusters for large-scale dynamics and climate. *Journal of the Atmospheric Sciences*, *41*(1), 113–121. https://doi.org/10.1175/1520-0469(1984)041h0113:SIOTMCi2.0.CO;2

Heymsfield, G. M., & Schotz, S. (1985). Structure and evolution of a severe squall line over Oklahoma. *Monthly Weather Review*, *113*(9), 1563–1589. https://doi.org/10.1175/1520-0493(1985)113h1563:SAEOASi2.0.CO;2

Houze, R. A. (2004). Mesoscale convective systems. *Reviews of Geophysics*, *42*, RG4003. https://doi.org/10.1029/2004RG000150

Houze Jr., R. A. (1977). Structure and dynamics of a tropical squall-line system. *Monthly Weather Review*, *105*(12), 1540–1567. https://doi.org/10.1175/1520-0493(1977)105h1540:SADOATi2.0.CO;2

Houze Jr., R. A. (1989). Observed structure of mesoscale convective systems and implications for large-scale heating. *Quarterly Journal of the Royal Meteorological Society*, *115*(487), 425–461. https://doi.org/10.1002/qj.49711548702

Houze Jr., R. A. (2018). 100 Years of research on mesoscale convective systems. *Meteorological Monographs*, *59*, 17.1–17.54. https://doi.org/10.1175/AMSMONOGRAPHS-D-18-0001.1

Jensen, M. P., Petersen, W. A., Bansemer, A., Bharadwaj, N., Carey, L. D., Cecil, D. J., et al. (2016). The midlatitude continental convective clouds experiment (MC3E). *Bulletin of the American Meteorological Society*, *97*(9), 1667–1686. https://doi.org/10.1175/BAMS-D-14-00228.1

Jensen, M. P., Toto, T., Troyan, D., Ciesielski, P. E., Holdridge, D., Kyrouac, J., et al. (2015). The midlatitude continental convective clouds experiment (MC3E) sounding network: Operations, processing and analysis. *Atmospheric Measurement Techniques*, *8*(1), 421–434. https://doi.org/10.5194/amt-8-421-2015

Johnson, R. H., & Hamilton, P. J. (1988). The relationship of surface pressure features to the precipitation and airflow structure of an intense midlatitude squall line. *Monthly Weather Review*, *116*(7), 1444–1473. https://doi.org/10.1175/1520-0493(1988)116h1444:TROSPFi2.0.CO;2

Kumar, V. V., Jakob, C., Protat, A., Williams, C. R., & May, P. T. (2015). Mass-flux characteristics of tropical cumulus clouds from wind profiler observations at Darwin, Australia. *Journal of the Atmospheric Sciences*, *72*(5), 1837–1855. https://doi.org/10.1175/JAS-D-14-0259.1

Lafore, J.-P., & Moncrieff, M. W. (1989). A numerical investigation of the organization and interaction of the convective and stratiform regions of tropical squall lines. *Journal of the Atmospheric Sciences*, *46*(4), 521–544. https://doi.org/10.1175/1520-0469(1989)046h0521:ANIOTOi2.0.CO;2

LeMone, M. A., & Zipser, E. J. (1980). Cumulonimbus vertical velocity events in GATE. Part I: Diameter, intensity and mass flux. *Journal of the Atmospheric Sciences*, *37*(11), 2444–2457. https://doi.org/10.1175/1520-0469(1980)037h2444:CVVEIGi2.0.CO;2

Leary, C. A., & Houze, R. A. (1979). The structure and evolution of convection in a tropical cloud cluster. *Journal of the Atmospheric Sciences*, *36*(3), 437–457. https://doi.org/10.1175/1520-0469(1979)036h0437:TSAEOCi2.0.CO;2

Lerach, D. G., Rutledge, S. A., Williams, C. R., & Cifelli, R. (2010). Vertical structure of convective systems during NAME 2004. *Monthly Weather Review*, *138*(5), 1695–1714. https://doi.org/10.1175/2009MWR3053.1

Leutwyler, D., Fuhrer, O., Lapillonne, X., Lüthi, D., & Schär, C. (2016). Towards European-scale convection-resolving climate simulations with GPUs: A study with COSMO 4.19. *Geoscientific Model Development*, *9*(9), 3393–3412. https://doi.org/10.5194/gmd-9-3393-2016

Lucas, C., Zipser, E. J., & LeMone, M. A. (1994). Convective available potential energy in the environment of oceanic and continental clouds: Correction and comments. *Journal of the Atmospheric Sciences*, *51*(24), 3829–3830. https://doi.org/10.1175/1520-0469(1994)051h3829:CAPEITi2.0.CO;2

Lucas, C., Zipser, E. J., & Lemone, M. A. (1994). Vertical velocity in oceanic convection off tropical Australia. *Journal of the Atmospheric Sciences*, *51*(21), 3183–3193. https://doi.org/10.1175/1520-0469(1994)051h3183:VVIOCOi2.0.CO;2

Machado, L. A. T., Laurent, H., Dessay, N., & Miranda, I. (2004). Seasonal and diurnal variability of convection over the Amazonia: A comparison of different vegetation types and large scale forcing. *Theoretical and Applied Climatology*, *78*(1), 61–77. https://doi.org/10.1007/s00704-004-0044-9

Mapes, B., Tulich, S., Lin, J., & Zuidema, P. (2006). The mesoscale convection life cycle: Building block or prototype for large-scale tropical waves? *Dynamics of Atmospheres and Oceans*, *42*(1), 3–29. https://doi.org/10.1016/j.dynatmoce.2006.03.003

Martin, S. T., Artaxo, P., Machado, L. A. T., Manzi, A. O., Souza, R. A. F., Schumacher, C., et al. (2016). Introduction: Observations and Modeling of the Green Ocean Amazon (GoAmazon2014/5). *Atmospheric Chemistry and Physics*, *16*(8), 4785–4797. https://doi.org/10.5194/acp-16-4785-2016

Martin, S. T., Artaxo, P., Machado, L., Manzi, A. O., Souza, R. A. F., Schumacher, C., et al. (2017). The Green Ocean Amazon experiment (GoAmazon2014/5) observes pollution affecting gases, aerosols, clouds, and rainfall over the rain forest. *Bulletin of the American Meteorological Society*, *98*(5), 981–997. https://doi.org/10.1175/BAMS-D-15-00221.1

Mather, J. H., & Voyles, J. W. (2013). The arm climate research facility: A review of structure and capabilities. *Bulletin of the American Meteorological Society*, *94*(3), 377–392. https://doi.org/10.1175/BAMS-D-11-00218.1

May, P. T., Jameson, A. R., Keenan, T. D., Johnston, P. E., & Lucas, C. (2002). Combined wind profiler/polarimetric radar studies of the vertical motion and microphysical characteristics of tropical sea-breeze thunderstorms. *Monthly Weather Review*, *130*(9), 2228–2239. https://doi.org/10.1175/1520-0493(2002)130h2228:CWPPRSi2.0.CO;2

May, P. T., & Keenan, T. D. (2005). Evaluation of microphysical retrievals from polarimetric radar with wind profiler data. *Journal of Applied Meteorology*, *44*(6), 827–838. https://doi.org/10.1175/JAM2230.1

May, P. T., & Rajopadhyaya, D. K. (1996). Wind profiler observations of vertical motion and precipitation microphysics of a tropical squall line. *Monthly Weather Review*, *124*(4), 621–633. https://doi.org/10.1175/1520-0493(1996)124h0621:WPOOVMi2.0.CO;2

May, P. T., & Rajopadhyaya, D. K. (1999). Vertical velocity characteristics of deep convection over Darwin, Australia. *Monthly Weather Review*, *127*(6), 1056–1071. https://doi.org/10.1175/1520-0493(1999)127h1056:VVCODCi2.0.CO;2

Miller, M. A., Nitschke, K., Ackerman, T. P., Ferrell, W. R., Hickmon, N., & Ivey, M. (2016). The ARM Mobile Facilities. *Meteorological Monographs*, *57*, 9.1–9.15. https://doi.org/10.1175/AMSMONOGRAPHS-D-15-0051.1

Moncrieff, M. W. (1992). Organized convective systems: Archetypal dynamical models, mass and momentum flux theory, and parametrization. *Quarterly Journal of the Royal Meteorological Society*, *118*(507), 819–850. https://doi.org/10.1002/qj.49711850703

Morrison, H., Thompson, G., & Tatarskii, V. (2009). Impact of cloud microphysics on the development of trailing stratiform precipitation in a simulated squall line: Comparison of one- and two-moment schemes. *Monthly Weather Review*, *137*(3), 991–1007. https://doi.org/10.1175/2008MWR2556.1

Mrowiec, A. A., Rio, C., Fridlind, A. M., Ackerman, A. S., Del Genio, A. D., Pauluis, O. M., et al. (2012). Analysis of cloud-resolving simulations of a tropical mesoscale convective system observed during TWP-ICE: Vertical fluxes and draft properties in convective and stratiform regions. *Journal of Geophysical Research*, *117*, D19201. https://doi.org/10.1029/2012JD017759

Nesbitt, S. W., Cifelli, R., & Rutledge, S. A. (2006). Storm morphology and rainfall characteristics of TRMM precipitation features. *Monthly Weather Review*, *134*(10), 2702–2721. https://doi.org/10.1175/MWR3200.1

North, K. W., Oue, M., Kollias, P., Giangrande, S. E., Collis, S. M., & Potvin, C. K. (2017). Vertical air motion retrievals in deep convective clouds using the ARM scanning radar network in Oklahoma during MC3E. *Atmospheric Measurement Techniques*, *10*(8), 2785–2806. https://doi.org/10.5194/amt-10-2785-2017

Parker, M. D., & Johnson, R. H. (2000). Organizational modes of midlatitude mesoscale convective systems. *Monthly Weather Review*, *128*(10), 3413–3436. https://doi.org/10.1175/1520-0493(2001)129h3413:OMOMMCi2.0.CO;2

Parker, M. D., & Johnson, R. H. (2004). Simulated convective lines with leading precipitation. Part I: Governing dynamics. *Journal of the Atmospheric Sciences*, *61*(14), 1637–1655. https://doi.org/10.1175/1520-0469(2004)061h1637:SCLWLPi2.0.CO;2

Prein, A. F., Liu, C., Ikeda, K., Bullock, R., Rasmussen, R. M., Holland, G. J., & Clark, M. (2017). Simulating North American mesoscale convective systems with a convection-permitting climate model. *Climate Dynamics*, *49*, 1–16. https://doi.org/10.1007/s00382-017-3993-2

Rasmussen, E. N., Straka, J. M., Davies-Jones, R., Doswell, C. A., Carr, F. H., Eilts, M. D., & MacGorman, D. R. (1994). Verification of the origins of rotation in tornadoes experiment: Vortex. *Bulletin of the American Meteorological Society*, *75*(6), 995–1006. https://doi.org/10.1175/1520-0477(1994)075h0995:VOTOORi2.0.CO;2

Roca, R., Aublanc, J., Chambon, P., Fiolleau, T., & Viltard, N. (2014). Robust observational quantification of the contribution of mesoscale convective systems to rainfall in the tropics. *Journal of Climate*, *27*(13), 4952–4958. https://doi.org/10.1175/JCLI-D-13-00628.1

Romatschke, U., & Houze, R. A. (2010). Extreme summer convection in South America. *Journal of Climate*, *23*(14), 3761–3791. https://doi.org/10.1175/2010JCLI3465.1

Rotunno, R., Klemp, J. B., & Weisman, M. L. (1988). A theory for strong, long-lived squall lines. *Journal of the Atmospheric Sciences*, *45*(3), 463–485. https://doi.org/10.1175/1520-0469(1988)045h0463:ATFSLLi2.0.CO;2

Roux, F. (1988). The West African squall line observed on 23 June 1981 during COPT 81: Kinematics and thermodynamics of the convective region. *Journal of the Atmospheric Sciences*, *45*(3), 406–426. https://doi.org/10.1175/1520-0469(1988)045h0406:TWASLOi2.0.CO;2

Sanderson, B. M., Piani, C., Ingram, W. J., Stone, D. A., & Allen, M. R. (2008). Towards constraining climate sensitivity by linear analysis of feedback patterns in thousands of perturbed-physics GCM simulations. *Climate Dynamics*, *30*(2), 175–190. https://doi.org/10.1007/s00382-007-0280-7

Schiro, K. A., & Neelin, J. D. (2018). Tropical continental downdraft characteristics: Mesoscale systems versus unorganized convection. *Atmospheric Chemistry and Physics*, *18*(3), 1997–2010. https://doi.org/10.5194/acp-18-1997-2018

Schumacher, C., Houze, R. A., & Kraucunas, I. (2004). The tropical dynamical response to latent heating estimates derived from the TRMM precipitation radar. *Journal of the Atmospheric Sciences*, *61*(12), 1341–1358. https://doi.org/10.1175/1520-0469(2004)061h1341:TTDRTLi2.0.CO;2

Sherwood, S. C., Bony, S., & Dufresne, J.-L. (2014). Spread in model climate sensitivity traced to atmospheric convective mixing. *Nature*, *505*, 37–42.

Silva Dias, M. A. F., Rutledge, S., Kabat, P., Silva Dias, P. L., Nobre, C., Fisch, G., et al. (2002). Cloud and rain processes in a biosphere-atmosphere interaction context in the Amazon region. *Journal of Geophysical Research*, *107*(D20), 8072. https://doi.org/10.1029/2001JD000335

Sisterson, D. L., Peppler, R. A., Cress, T. S., Lamb, P. J., & Turner, D. D. (2016). The ARM Southern Great Plains (SGP) site. *Meteorological Monographs*, *57*, 6.1–6.14. https://doi.org/10.1175/AMSMONOGRAPHS-D-16-0004.1

Skamarock, W. C., Park, S.-H., Klemp, J. B., & Snyder, C. (2014). Atmospheric kinetic energy spectra from global high-resolution nonhydrostatic simulations. *Journal of the Atmospheric Sciences*, *71*(11), 4369–4381. https://doi.org/10.1175/JAS-D-14-0114.1

Skamarock, W. C., Weisman, M. L., & Klemp, J. B. (1994). Three-dimensional evolution of simulated long-lived squall lines. *Journal of the Atmospheric Sciences*, *51*(17), 2563–2584. https://doi.org/10.1175/1520-0469(1994)051h2563:TDEOSLi2.0.CO;2

Smull, B. F., & Houze, R. A. (1987). Rear inflow in squall lines with trailing stratiform precipitation. *Monthly Weather Review*, *115*(12), 2869–2889. https://doi.org/10.1175/1520-0493(1987)115h2869:RIISLWi2.0.CO;2

Stith, J. L., Haggerty, J. A., Heymsfield, A., & Grainger, C. A. (2004). Microphysical characteristics of tropical updrafts in clean conditions. *Journal of Applied Meteorology*, *43*(5), 779–794. https://doi.org/10.1175/2104.1

Trenberth, K. E., Fasullo, J. T., & Kiehl, J. (2009). Earth's global energy budget. *Bulletin of the American Meteorological Society*, *90*(3), 311–324. https://doi.org/10.1175/2008BAMS2634.1

Tridon, F., Battaglia, A., Kollias, P., Luke, E., & Williams, C. R. (2013). Signal postprocessing and reflectivity calibration of the atmospheric radiation measurement 915-MHz wind profilers. *Journal of Atmospheric and Oceanic Technology*, *30*, 1038–1054.

Trier, S. B., & Sharman, R. D. (2009). Convection-permitting simulations of the environment supporting widespread turbulence within the upper-level outflow of a mesoscale convective system. *Monthly Weather Review*, *137*(6), 1972–1990. https://doi.org/10.1175/2008MWR2770.1

Varble, A., Zipser, E. J., Fridlind, A. M., Zhu, P., Ackerman, A. S., Chaboureau, J.-P., et al. (2014). Evaluation of cloud-resolving and limited area model intercomparison simulations using TWP-ICE observations: 1. Deep convective updraft properties. *Journal of Geophysical Research: Atmospheres*, *119*, 13,891–13,918. https://doi.org/10.1002/2013JD021371

Vescio, M. D., & Johnson, R. H. (1992). The surface-wind response to transient mesoscale pressure fields associated with squall lines. *Monthly Weather Review*, *120*(9), 1837–1850. https://doi.org/10.1175/1520-0493(1992)120h1837:TSWRTTi2.0.CO;2

Wang, D., Giangrande, S. E., Bartholomew, M. J., Hardin, J., Feng, Z., Thalman, R., & Machado, L. A. T. (2018). The Green Ocean: Precipitation insights from the GoAmazon2014/5 experiment. *Atmospheric Chemistry and Physics*, *18*(12), 9121–9145. https://doi.org/10.5194/acp-18-9121-2018

Williams, C. R. (2012). Vertical air motion retrieved from dual-frequency profiler observations. *Journal of Atmospheric and Oceanic Technology*, *29*(10), 1471–1480. https://doi.org/10.1175/JTECH-D-11-00176.1

Williams, C. R., Ecklund, W. L., & Gage, K. S. (1995). Classification of precipitating clouds in the tropics using 915-MHz wind profilers. *Journal of Atmospheric and Oceanic Technology*, *12*(5), 996–1012. https://doi.org/10.1175/1520-0426(1995)012h0996:COPCITi2.0.CO;2

Yuter, S. E., & Houze, R. A. Jr. (1995a). Three-dimensional kinematic and microphysical evolution of Florida cumulonimbus. Part II: Frequency distributions of vertical velocity, reflectivity, and differential reflectivity. *Monthly Weather Review*, *123*, 1941–1963. https://doi.org/10.1175/1520-0493(1995)123<1941:TDKAME>2.0.CO;2

Yuter, S. E., & Houze, R. A. Jr. (1995b). Three-dimensional kinematic and microphysical evolution of Florida cumulonimbus. Part III: Vertical mass transport, mass divergence, and synthesis. *Monthly Weather Review*, *123*(7), 1964–1983. https://doi.org/10.1175/1520-0493(1995)123<1964:TDKAME>2.0.CO;2

Zipser, E. J. (1969). The role of organized unsaturated convective downdrafts in the structure and rapid decay of an equatorial disturbance. *Journal of Applied Meteorology*, *8*(5), 799–814. https://doi.org/10.1175/1520-0450(1969)008h0799:TROOUCi2.0.CO;2

Zipser, E. J. (1977). Mesoscale and convective-scale downdrafts as distinct components of squall-line structure. *Monthly Weather Review*, *105*(12), 1568–1589. https://doi.org/10.1175/1520-0493(1977)105h1568:MACDADi2.0.CO;2

Zipser, E. J. (2003). Some views on "hot towers" after 50 years of tropical field programs and two years of TRMM data. *Meteorological Monographs*, *51*, 49–58. https://doi.org/10.1175/0065-9401(2003)029h0049:CSVOHTi2.0.CO;2

Zipser, E. J., & Lutz, K. R. (1994). The vertical profile of radar reflectivity of convective cells: A strong indicator of storm intensity and lightning probability? *Monthly Weather Review*, *122*(8), 1751–1759. https://doi.org/10.1175/1520-0493(1994)122h1751:TVPORRi2.0.CO;2